This is a repository copy of *Design and implementation of a non-resonant vibration-assisted machining device to create bespoke surface textures*.

White Rose Research Online URL for this paper:
http://eprints.whiterose.ac.uk/94583/

Version: Accepted Version

**Article:**

# Design and Implementation of a Non-Resonant Vibration Assisted Machining Device to Create Bespoke Surface Textures

H. Suzuki,[*] M. B. Marshall, N. D. Sims, and R. S. Dwyer-Joyce

Department of Mechanical Engineering, The University of Sheffield, Mappin Street, Sheffield S1 3JD, UK.

## Abstract

Non-resonant vibration assisted machining involves the superposition of controlled vibrations onto traditional machining processes such as turning or milling. In this study, a novel variant of this technique has been investigated using an off-the-shelf piezoelectric actuator to create bespoke surface textures in a conventional milling machine. The purpose of these surfaces is to provide enhanced tribological performance by reserving lubricant, trapping and discharging debris and wear particles, and delaying the collapse of the full hydrodynamic lubricant film. Surface textures consisting of a repeating radial striation pattern of sine waves were reproducibly generated on the face of the disc work piece (an aluminium alloy 6082 and a low-alloyed steel 16MnCr5) when the frequency of the superposed vibration was in phase with the rotational speed of the work piece. The texture parameters were controllable from approximately 1 mm to 8 mm in the wavelength and from a few microns to 25 $\mu$m in the peak to peak amplitudes which would reasonably cover the range of hydrodynamic lubrication film thickness.

## 1  Introduction

In respect of tribological performance in the hydrodynamic lubrication regime, it has been shown that bespoke surface textures work beneficially by; creating a lubricant reservoir[1], debris and wear particle trapping and discharge[2], and a micro-bearing effect generating additional hydrodynamic pressure[3,4] that could prevent the collapse of the full hydrodynamic lubricant film. There are several techniques available to fabricate such surface textures: (i) overlaying techniques which provide an additional layer on the substrate

---

[*]Corresponding author. Tel: +44 114 222 5507. E-mail address: hiroyuki.suzuki@sheffield.ac.uk

such as; chemical vapour deposition[5], physical vapour deposition[6], electro deposition[7], inkjet printing[8], or laser micro cladding methods[9]; (ii) subtractive techniques which form recesses or depressions removing out the material on the substrate such as; traditional machining[10], photolithography and reactive ion etching[11], electrical discharge[12], ion beam[13], or laser based methods[14]; (iii) deforming techniques which create plastic deformations on the substrate such as; shot peening[15] or fine particle bombardment methods[16]. All of the above techniques are finishing processes applied after the initial machining and therefore are only economically viable in limited applications.

Vibration assisted machining involves the superposition of controlled vibrations onto traditional machining processes such as turning or milling. These machining techniques can be categorised into two by the means of vibration generation[17]; (i) resonant technique where a sonotrode (also called horn or concentrator) vibrates at its natural frequency transferring and amplifying a given vibration from a vibration source (usually by magnetostrictive or piezoelectric transducer), or (ii) non-resonant technique where a piezoelectric material vibrates below its first natural frequency driven by an amplified dynamic voltage. The resonant techniques have been implemented mainly for improved surface profile or roughness, burr suppression, cutting force reduction, or longer cutting tool life[18–22]. However, there exists a limitation in the resonant technique that the operating vibration parameters, frequency and displacement, are inherently fixed in a given design, by which the machining conditions available could be limited. The beneficial points of the non-resonant technique are the controllability of vibration parameters in a given design, and the good displacement uniformity and resolution. The non-resonant techniques have been examined for the purposes as mentioned in the resonant technique[23,24] as well as for creating bespoke surface textures[25].

Greco et al[25] investigated the potential of a non-resonant vibration assisted machining technique (termed Vibromechanical texturing) to create bespoke surfaces for tribological interfaces. A piezoelectric-actuated tool and positioning stage (developed by Hong et al[26]) were used to superpose controlled vibrations on to a cutting tool normal to the work piece surface. The intermittent engagement of the cutter to the surface created dimples in aluminium and hardened steel work pieces, however, the errors between the desired profiles and the profiles generated were large, particularly in the hardened steel work piece. The authors concluded that the inaccuracy was attributed to elastic restoration of the material and deflection of the positioning stage, which are inherently present in the chosen arrangement. A further issue arose from burr generations in the diverging edge of the generated dimples, which required an additional removal process. It is presumed that the burrs were generated due to the intermittent engagement of the cutting tool.

This study aims to develop a non-resonant vibration assisted machining device to create bespoke surface textures accurately, and minimise the aforementioned issues of elastic deflection and burr generation. A novel device design is proposed to superimpose controlled vibrations on to a cutting tool normal to the work piece surface using an off-the-shelf piezoelectric actuator. The mechanical assembly is designed to achieve high axial mechanical stiffness so that elastic deflection as a consequence of the cutting process is limited. The constructed device is validated experimentally using disc work pieces in a conventional milling machine. During the machining operation with superimposed vibration, the tool is continuously engaged

with the face of the disc in order to suppress burr generation, allowing the surface texture to be embedded at the same time as the finish cut is performed.

# 2 Development of a Non-Resonant Vibration Assisted Machining Device

In summary, there exists several design parameters to be considered to achieve the feasible design of the non-resonant vibration assisted machining device in the desired operation range. Hydrodynamic oil films are generally formed in the thickness range from a few $\mu$m to 30 $\mu$m, thus the displacement range of the actuator needs to be of that order. The actuator needs to have suitable force capacities to drive the cutting tool with forces by the cutting process. Then, an electrically suitable amplifier should be selected to excite the selected actuator. In the mechanical arrangement, the mass driven by the actuator is a critical parameter as the mass would determine the resonant frequency and dynamic force in the dynamic operation. As well as the high axial mechanical stiffness of the assembly to avoid the undesired elastic deflection, a protective measure is necessary such that the piezoelectric element of the actuator is not exposed to the shear or twist forces which would be generated by the cutting process.

## 2.1 Piezoelectric Actuator and Amplifier Selection

### 2.1.1 Piezoelectric actuator

A piezoelectric (lead zirconate titanate (PZT)) actuator (P-212.40 from Physik Instrumente (PI) GmbH & Co) with a displacement and a force capacity was selected as summarised in Table 1. The push force of piezoelectric actuator, $F_{\text{push}}$, is generated by the piezoelectric element by its piezoelectric effect, interacting with a preload spring installed on the top of the piezoelectric element. The piezoelectric actuator can generate a maximum push force when displacement of piezoelectric actuator, $\Delta L$, is zero, and can travel a maximum displacement with zero force generation in an applied operating voltage of piezoelectric element, $V_{\text{e}}$, as summarised in Figure 1. Maximum push force of the actuator, i.e. push force capacity of piezoelectric actuator, $F'_{\text{push}}$, is generated with zero displacement when maximum operating voltage, 1000 V is applied. The pull force of the piezoelectric actuator, $F_{\text{pull}}$, is generated by the preload spring and its capacity, $F'_{\text{pull}}$, is set at 300 N. Inherently the piezoelectric element is not able to generate the negative force (pull force) as the piezoelectric element, especially the electrode layer, is very vulnerable to tensile stress. The stiffness of the piezoelectric actuator, $\kappa_{\text{a}}$, is 33.3 N/$\mu$m, determined by interaction of the stiffness of the piezoelectric element and the stiffness of the preload spring. $\kappa_{\text{a}}$ is not a mechanical stiffness of the piezoelectric actuator, as it is the ratio of the push force generation and its according displacement range of the piezoelectric element, $\Delta L_{\text{r}}$, with an operating voltage by its piezoelectric effect (or simply $F'_{\text{push}}/\Delta L'$).

Table 1: Specification of actuator, P-212.40 of PI[27].

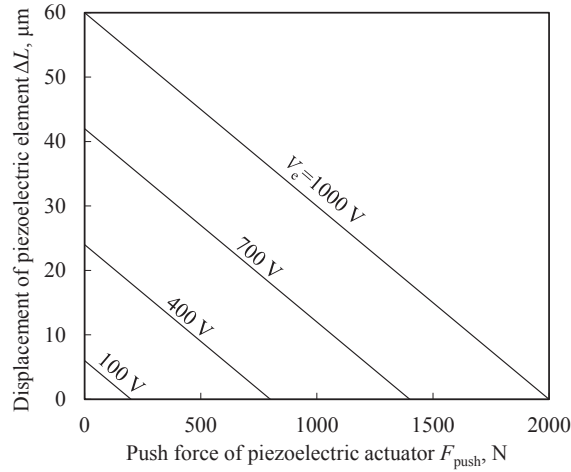| Operating voltage $V_e$ | V | 0 to 1000 |
|---|---|---|
| Displacement capacity $\Delta L'$ | $\mu$m | 60 |
| Push force capacity $F'_{push}$ | N | 2000 |
| Pull force capacity $F'_{pull}$ | N | 300 |
| Capacitance | nF | 180 |
| Stiffness $\kappa_a$ | N/$\mu$m | 33.3 |
| Mass of piezoelectric element $m$ | grams | 35 |
| Operating temperature | °C | -40 to +80 |



Figure 1: $F_{push}$ and $\Delta L$ variation with the operating voltage of P-212.40[27].

### 2.1.2 Amplifier

An amplifier which suited the excitation of this actuator was chosen. The amplifier selected (E-481 from Physik Instrumente (PI) GmbH & Co) is a high-power amplifier designed specifically for dynamic operation of high-capacitance PZT actuators. The output voltage is from 0 V to 1100 V with a voltage gain of 100. The main specification is summarised in Table 2. The selected actuator (P-212.40) with E-481 can be driven in either open-loop or closed-loop operation. In this study open-loop was used as the operation required a faster response than closed-loop can achieve, in particular, in test conditions with a high required frequency range.

Table 2: Specification of amplifier, E-481 of PI[28].

| | | |
|---|---|---|
| Voltage gain | - | 100 |
| Output voltage | V | 0 to 1100 |
| Output current average | mA | >600 |
| Output current peak | mA | 2000 |
| Output power average | VA | 630 |
| Output power peak | VA | 2000 |

## 2.2 Mechanical Arrangement

In this study the constructed device is arranged in a conventional milling machine for the simplicity of the arrangement. The disc work piece (an aluminium alloy 6082 and a low-alloyed steel 16MnCr5) is set in the milling machine spindle and the mechanical assembly on the milling machine stage to turn the face of the work piece. The work piece represents the counterpart of a tilting pad thrust bearing used in a production gas turbine engine, as summarised in Table 3.

Table 3: Specifications of work pieces.

| | | |
|---|---|---|
| Machined outer diameter | mm | 136 |
| Machined inner diameter | mm | 84 |
| Aluminium alloy 6082 | | |
| Vickers hardness | MPa | 1216 |
| Heat treatment/finish | - | Solution heat |
| Specific cutting force $K_s$ | MPa | 2100 incl. SF |
| Low-alloyed steel 16MnCr5 | | |
| Vickers hardness | MPa | 2491 |
| Heat treatment/finish | - | Cold drawn |
| Specific cutting force $K_s$ | MPa | 5100 incl. SF |

### 2.2.1 Mechanical assembly

Figure 2 shows the mechanical arrangement of the device developed for this study. The height of the assembly is 199 mm from the base plate to the cutter insert tip and the outer diameter of the housing is 80 mm. The selected actuator is rigidly bolted against a conventional cutting tool. The vibration is transmitted through the cutter (cutter insert and cutter shank) normal to the face of the work piece. The cutter and the actuator are secured in the housing and the base plate which is bolted on the milling machine stage. The cutter feeds in the radial direction with respect to the work piece, with its vertical position also controlled and set at the start of a machining test. A roller bearing guides the vibration and supports the bending force acting on the cutter insert, and the pin supports the twisting force from the cutting process, so that the shear stress is not transmitted to the piezoelectric element that makes up the actuator. The flexible tip (P-176.60 from Physik Instrumente (PI) GmbH & Co) set between the cutter shank and the actuator is flexible mainly

to the bending direction due to the notches arranged on the surface. This flexible tip further reduces the stress on the piezoelectric element induced by the bending force acting on the cutter insert, and the bending force which might occur through misalignment between the actuator and the cutter shank when assembled. Specific cutting forces, $K_s$, including a safety factor (SF) of 3.0 were selected as summarised in Table 3 [29].
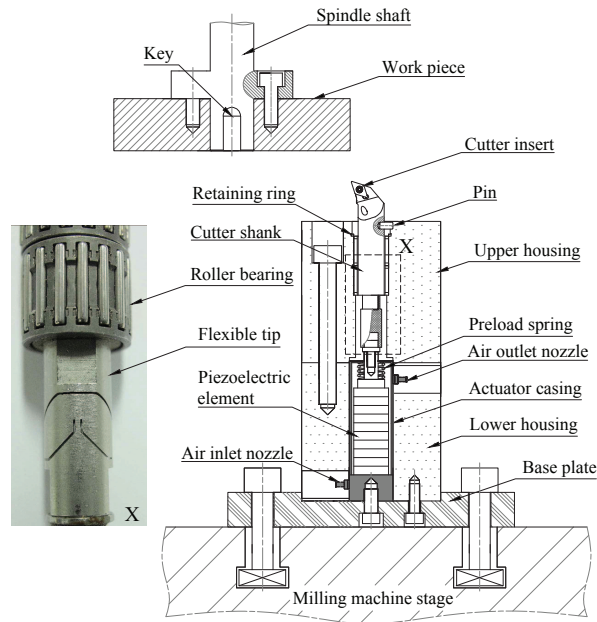


Figure 2: Mechanical arrangement.

### 2.2.2 Cutter shank and insert

The cutter shank (CoroTurn 107 from Sandvik Coromant) and the cutter insert (DCET 07 02 01-UM 1125 from Sandvik Coromant) were selected on the basis of mass and cutter insert edge radius. The shank and insert masses are critical because this mass contributes to the dynamic force of vibration which limits the operation range. The smallest edge radius of the cutter insert available was chosen to generate the surface textures with good geometrical resolution. The main specifications of the selected cutter insert are summarised in Figure 3.
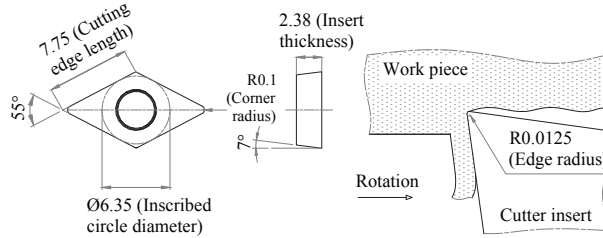
6

Figure 3: Specifications of cutter insert, DCET 07 02 01-UM 1125, from Sandvik Coromant[29].

## 2.3    Electrical Control and Air Cooling Arrangement

The piezoelectric element is excited by a voltage source unit (NI-USB-9263 from National Instruments) amplified by the amplifier (E-481). The displacement signal of the piezoelectric element via a strain gauge (strain gauge (a)) and the operating voltage of piezoelectric element are monitored by a voltage monitor unit (NI-USB-6008 from National Instruments) as shown in Figure 4. An apparent strain caused by a resistance change of the strain gauge (a) over the temperature change of the piezoelectric element is compensated using a Wheatstone bridge circuit with another strain gauge (strain gauge (b)) which is also placed on the piezoelectric element. The parameters of the vibration are commanded by a control PC. The possible vibration wave forms include sine wave, triangle wave, square wave, and saw tooth wave. In this study the sine wave was exclusively used to obtain tribologically optimised surfaces. The heat that the piezoelectric element generates in dynamic operation is dissipated by compressed air which is controlled down to 0.5 bar through a dryer, filter and air regulator (MSB6 from Festo). The temperature of the piezoelectric element is monitored through a thermocouple placed on the piezoelectric element with a fail-safe set should the temperature exceed 80 °C, which is the operating limit of the piezoelectric element.
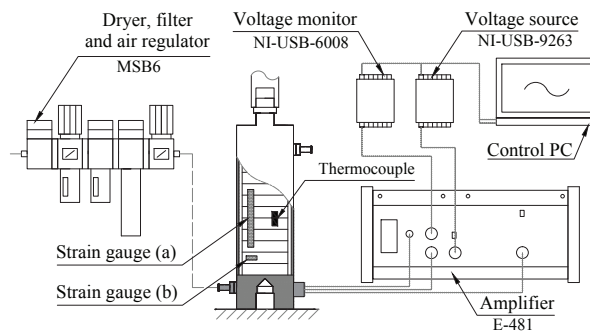


Figure 4: Electrical Control and Air Cooling Arrangement.

## 2.4 Operating Regimes

In a dynamic operation where the cutter vibrates perpendicular to the work piece at a given frequency and displacement, the mass-spring system of the developed assembly interacts with friction forces incurred by the contacts (e.g. between the roller bearings and the cutter shank or the pin and the housing slot), and cutting resistance i.e. the cutting force of the work piece. In respect of the feasibility of a dynamic operation the friction forces are considered to be negligibly small. The piezoelectric element generating the pushing force and the preload spring generating the pulling force are considered to be a spring element of the system. The coordinate $x$, $y$, and $z$ is set as shown in Figure 5. The $x$ coordinate is the tangential direction of the disc work piece, the $y$ coordinate is the radial direction of the disc work piece, and the $z$ coordinate is the vibration direction, i.e. the axial direction of the cutter shank, respectively.

### 2.4.1 Cutting force

The cutting force is a force generated from the contact between the cutter insert and the work piece. It is assumed that the cutting of the spinning work piece with a feeding cutter can be approximated as a three-dimensional turning operation of infinite work piece diameter. Since the cutter engages with the work piece continuously along the sinusoidal displacement, the cutting could be considered as a conventional cutting engagement with a varying depth of cut. Therefore, the generated cutting force acting on the cutter can be divided into three components; tangential force of cutting, $F_t$, feed force of cutting, $F_f$, and normal force of cutting, $F_n$, as shown in Figure 5. The cutting force varies with operational conditions such as cutting speed, feed speed, depth of cut, interfacial friction, and material properties[30]. Although it is difficult to deduce these force components accurately, a suitable simplification[31] is that the ratio of each component remains constant for all operating conditions as:

$$F_t = K_s A, \tag{1}$$

$$F_t : F_n : F_f \approx 10 : 3 : 1, \tag{2}$$

where $K_s$ is the specific cutting force (a force per unit area), and $A$ is the area of the chip. $A$ can be expressed as follows:

$$A = u_{fpr} t_d, \tag{3}$$

where $u_{fpr}$ is feed per revolution and $t_d$ is the depth of cut. $u_{fpr}$ is given as:

$$u_{fpr} = \frac{u_f}{\omega}, \tag{4}$$

where $u_f$ is the feed speed of milling machine stage and $\omega$ is the rotation speed of spindle (work piece). As mentioned in the section describing the mechanical arrangement, only the normal force of cutting interacts

with the vibration since the tangential force and feed force of cutting are decoupled by the roller bearing. $F_n$ can be rearranged with Equations (1) to (4) as:

$$F_n = -\frac{3}{10}\frac{u_f}{\omega}K_s t_d,\tag{5}$$

where $t_d$ is a function of time, $t$, and varies with sinusoidal displacement, so it can be expressed as:

$$t_d(t) = \frac{\Delta L_{rt}}{2}\sin 2\pi f t + t_0,\tag{6}$$

where $t_0$ is initial depth of cut before the vibration is commanded and $\Delta L_{rt}$ is displacement range of cutter tip as seen in Figure 6. It is assumed that $\Delta L_{rt}$ and the measured displacement range of the piezoelectric element, $\Delta L_{rm}$, are approximately equal as the cutter and piezoelectric element is rigidly bolted and the elastic deformation of the cutter during cutting is negligibly small in the conducted conditions. Therefore Equations (5) and (6) can be rearranged as:

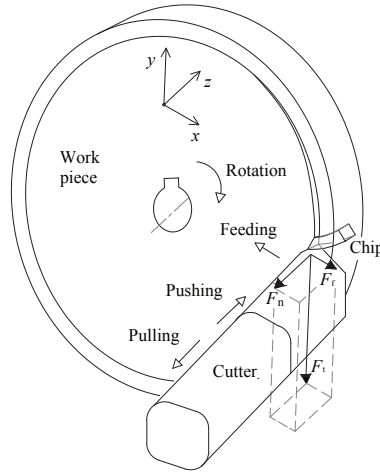$$F_n(t) = -\frac{3}{10}\frac{u_f}{\omega}K_s\left[t_0 + \frac{\Delta L_{rm}}{2}\sin 2\pi f t\right].\tag{7}$$



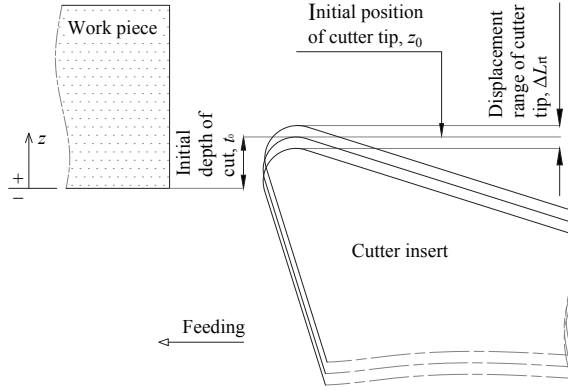Figure 5: Schematic of the motion of the cutter and work piece, and forces acting on the cutter.

Figure 6: Schematic of the cutting parameters.

## 2.4.2 Operation limits of vibration with cutting

With an approximation that the damping element in this mass-spring system is negligibly small, the motion of a dynamic operation in steady state can be described by:

$$m_{\text{eff}}\ddot{z}_{\text{c}}(t) + (\kappa_{\text{sp}} + \kappa_{\text{e}})z_{\text{c}}(t) = F_{\text{n}}(t), \tag{8}$$

where $z_{\text{c}}$ is the dynamic position of cutter tip in the $z$ coordinate, $\kappa_{\text{sp}}$ is the stiffness of the preload spring, $\kappa_{\text{e}}$ is the stiffness of the piezoelectric element, $m_{\text{eff}}$ is effective mass of the moving parts. The effect of the gravitational acceleration could be neglected in the dynamics. $m_{\text{eff}}$ is given as[32]:

$$m_{\text{eff}} \approx \frac{m}{3} + M, \tag{9}$$

where $m$ is the mass of the piezoelectric element and $M$ is the mass driven by the piezoelectric actuator as summarised in Figure 7.
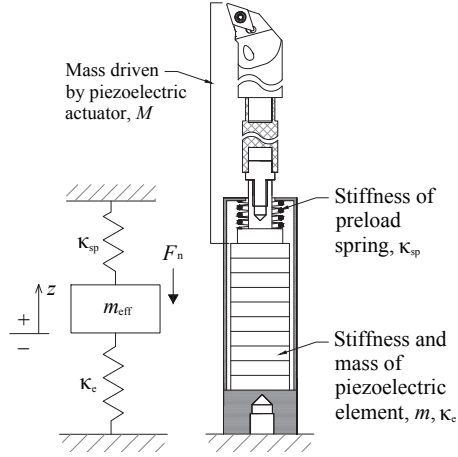
Figure 7: Schematic of force interactions between normal force of cutting and the actuator.

The preload spring is assumed to be of negligible mass. For a sinusoidal vibration, $z_c$ is given by:

$$z_c(t) = \frac{\Delta L_{rm}}{2} \sin 2\pi f t + z_0, \tag{10}$$

where $z_0$ is initial position of cutter tip in $z$ coordinate. Graphical representation in the time domain of Equation (8) at two conditions, **a** and **b** is presented in Figure 8. The parameters of the conditions are summarised in Table 4. The condition **a** represents a feasible operation and the condition **b** an unfeasible one. At both conditions it is noted that $m_{eff}\ddot{z}_c$ are predominantly greater than $F_n$ and $m_{eff}\ddot{z}_c$ yields greatest to the negative direction (point **A** and **B**) at the positive peak of $z_c$.
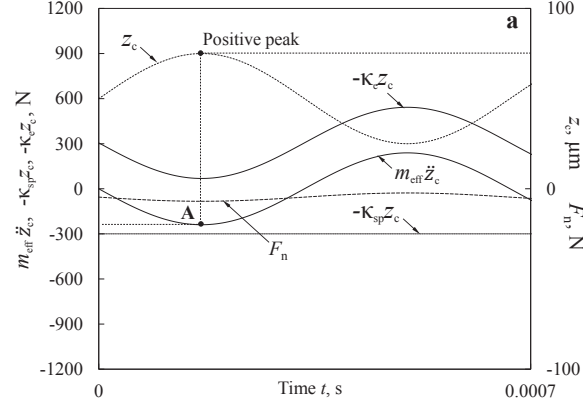
(a) At the condition **a**
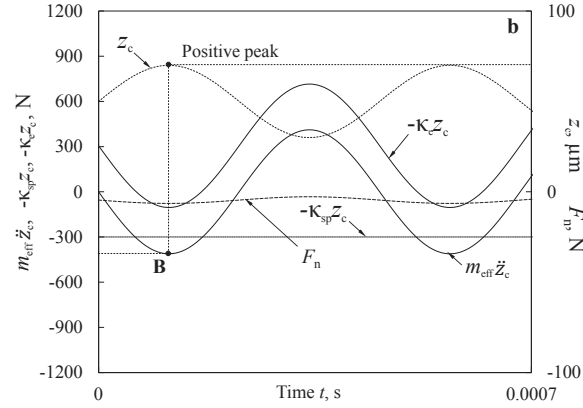


(b) At the condition **b**

Figure 8: Graphical representation of Equation (8).

Table 4: Parameters for the feasibility calculations.

| Symbol | Specific cutting force | Effective mass | Rotation speed of spindle | Feed speed | Initial depth of cut | Displacement range of piezo-electric element | Vibration frequency | Wave form |
|---|---|---|---|---|---|---|---|---|
| | $K_s$ | $m_{eff}$ | $\omega$ | $u_f$ | $t_0$ | $\Delta L_r$ | $f$ | |
| | MPa | grams | rpm | mm/s | $\mu$m | $\mu$m | Hz | |
| **a** | 5100 | 108 | 500 | 0.5 | 50 | 50 | 1500 | Sine |
| **b** | 5100 | 108 | 500 | 0.5 | 50 | 40 | 2200 | Sine |
| **c** | 5100 | 108 | 500 | 0.5 | 50 | 10 - 60 | 0 - 5000 | Sine |

Figure 9 shows $m_{eff}\ddot{z}_c$ at the conditions **a** and **b** with the force characteristics of the selected actuator over $\Delta L$. At the condition **a**, $m_{eff}\ddot{z}_c$ does not exceed either the $F_{push}$ line (at $V_e = 1000$ V) or the $F_{pull}$ line. In

contrast at the point **B** of the condition **b**, $m_{\text{eff}} \ddot{z}_{\text{c}}$ exceeds the $F_{\text{pull}}$ line while it does not exceed the $F_{\text{push}}$ line (at $V_{\text{e}} = 1000$ V) at the other end of the displacement. This is attributed to the force characteristics of the selected actuator where $F_{\text{pull}}$ is smaller than the usable $F_{\text{push}}$ while $V_{\text{e}} > 150$ V.
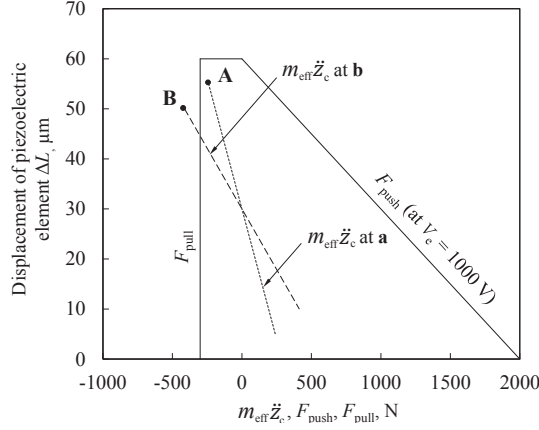


Figure 9: Deduced $m_{\text{eff}} \ddot{z}_{\text{c}}$ at the condition **a** and **b** with the force characteristics of the selected actuator.

It is noted that $\kappa_{\text{sp}} z_{\text{c}}$ is almost constant at a value of 300 N within the travel range of the piezoelectric element due to its small value of $\kappa_{\text{sp}}$. Therefore, as far as a suitable operating voltage is applied to the piezoelectric element, the operation limits of vibration would be determined by the dynamics at the positive peak of $z_{\text{c}}$ by substituting 300 N to $\kappa_{\text{sp}} z_{\text{c}}$ and 0 N to $\kappa_{\text{e}} z_{\text{c}}$ in Equation (8), that is:

$$m_{\text{eff}} \ddot{z}_{\text{c}}(t) - F_{\text{n}}(t) \geq -300. \tag{11}$$

The operation would be feasible while Equation (11) is satisfied within the range of the electrical operating limit of the amplifier and the range sufficiently below the first resonant frequency of the mass-spring system. The first resonant frequency, $f_{\text{res}}$, is given as [32]:

$$f_{\text{res}} = \frac{1}{2\pi} \sqrt{\frac{\kappa_{\text{a}}}{m_{\text{eff}}}}, \tag{12}$$

where $\kappa_{\text{a}}$ is stiffness of the selected actuator. In the constructed mass-spring system, $f_{\text{res}}$ was determined as 2.8 kHz by Equation (12). In order to investigate the limit of the pull force, a calculation for determining the feasible range of operation considering Equation (7) and (11) was carried out at the condition **c** as presented in Table 4. As summarised in Figure 10 two boundaries by the pull force limitation and the resonant frequency are shown. It is noted that this feasibility discussion can not be applied to machining tests with hard materials or with a deeper depth of cut where $F_{\text{n}}$ would be much greater, for which case the dynamics might be limited by $\kappa_{\text{e}} z_{\text{c}}$ rather than $\kappa_{\text{sp}} z_{\text{c}}$.
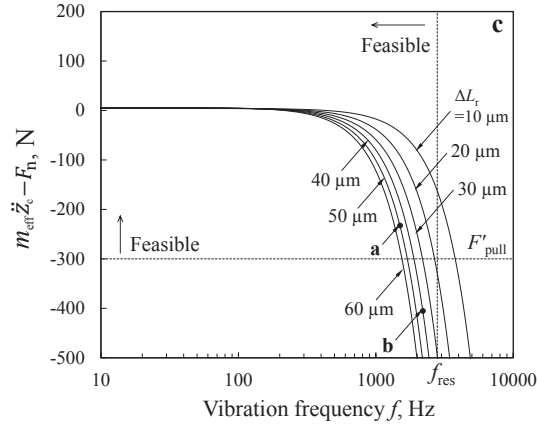
13

Figure 10: Feasible range of operation deduced at the condition **c**.

### 2.4.3   Preliminary actuation tests

Prior to the machining tests, actuation tests were carried out without engagement of the work piece to validate the design. The system is controlled by setting; mean voltage, $V_m$ (from 0 V to 10 V), voltage range, $\Delta V$ (from 0 V to 10 V), vibration frequency, $f$, and wave form (sinusoidal in this study). A LabVIEW interface was written to enter these parameters. Figure 11 shows the voltage range, $\Delta V$, compared with the displacement of the piezoelectric element as measured by the strain gauge, $\Delta L_{rm}$, in one of the conducted tests.
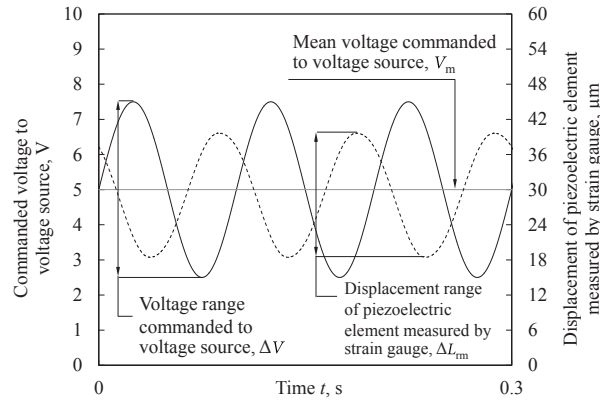


Figure 11: Displacement of piezoelectric element measured by the strain gauge and the commanded voltage in a 10 Hz open-loop operation without engagement to work piece.

The actuation tests were examined at six vibration frequencies, 1, 10, 100, 400, 800 and 1000 Hz, in the commanded voltage range, from 0 V to 10 V with the mean voltage 5 V. The results are summarized in Figure 12.
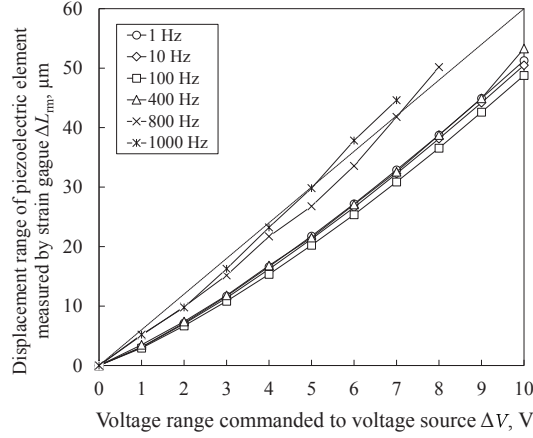
14

Figure 12: Summary of $\Delta L_{rm}$ with various operating frequencies at $V_m = 5$ V without engagement to work piece.

Overall the system was actuated well with good repeatability of displacements in all the test conditions with a phase shift between the driving voltage and the observed displacement. The measured displacement, $\Delta L_{rm}$, yielded greater when a higher vibration frequency was commanded in a commanded voltage range, $\Delta V$, e.g. the measured displacement was 25.4 $\mu$m at 400 Hz, 33.6 $\mu$m at 800 Hz, and 37.8 $\mu$m at 1000 Hz when the voltage range was commanded at 6 V. It is presumed that these measured displacement increased because the vibration frequency approached the first resonant frequency. The conditions with the large voltage ranges in 800 Hz and 1000 Hz were not tested as the operation became marginally unstable.

## 3 Experiment

### 3.1 Machining and Surface Measurement Procedure

The machining tests were examined at thirteen test conditions on the face of the disc work pieces with no cutting fluid. Table 5 shows the machining parameters and the commanded vibration parameters. The machining parameters, $\omega$, $u_f$, and $t_0$ were chosen on the basis of surface finish. The vibration parameter $\Delta V$ was chosen on the basis of the order of hydrodynamic lubrication film thickness (from a few $\mu$m to 30 $\mu$m generally) and then $f$ was set within the stably operable range confirmed in the preliminary actuation tests. In order to suppress the burr generation, the depth of cut was set so that the machining is continuously engaged to the work piece surface. Each work piece took 52 s to machine from the outer diameter of 136 mm to the inner diameter of 86 mm. These machining parameters and the commanded vibration parameters were not changed once set at start of a machining test until completed. Figure 13 schematically shows the generated surface features machined with vibration. Each of the work pieces was initially machined without vibration (i.e. conditions A1 and S1 for aluminium and steel, respectively).

15

Table 5: Machining test conditions.

| Work piece symbol | Material | Rotation speed of spindle | Feed speed | Initial depth of cut | Voltage range | Mean voltage | Vibration frequency | Wave form |
|---|---|---|---|---|---|---|---|---|
| | | $\omega$ | $u_f$ | $t_0$ | $\Delta V$ | $V_m$ | $f$ | |
| | | rpm | mm/s | $\mu$m | V | V | Hz | |
| A1 | Al 6082 | 200 | 0.5 | 50 | 0 | 5 | N/A | N/A |
| A2 | Al 6082 | 200 | 0.5 | 50 | 2 | 5 | 400 | Sine |
| A3 | Al 6082 | 200 | 0.5 | 50 | 4 | 5 | 400 | Sine |
| A4 | Al 6082 | 200 | 0.5 | 50 | 6 | 5 | 400 | Sine |
| A5 | Al 6082 | 200 | 0.5 | 50 | 4 | 5 | 800 | Sine |
| A6 | Al 6082 | 200 | 0.5 | 50 | 4 | 5 | 1000 | Sine |
| A7 | Al 6082 | 200 | 0.5 | 50 | 2 | 5 | 401 | Sine |
| S1 | 16MnCr5 | 500 | 0.5 | 50 | 0 | 5 | N/A | N/A |
| S2 | 16MnCr5 | 500 | 0.5 | 50 | 2 | 5 | 400 | Sine |
| S3 | 16MnCr5 | 500 | 0.5 | 50 | 4 | 5 | 400 | Sine |
| S4 | 16MnCr5 | 500 | 0.5 | 50 | 6 | 5 | 400 | Sine |
| S5 | 16MnCr5 | 500 | 0.5 | 50 | 4 | 5 | 800 | Sine |
| S6 | 16MnCr5 | 500 | 0.5 | 50 | 4 | 5 | 1000 | Sine |
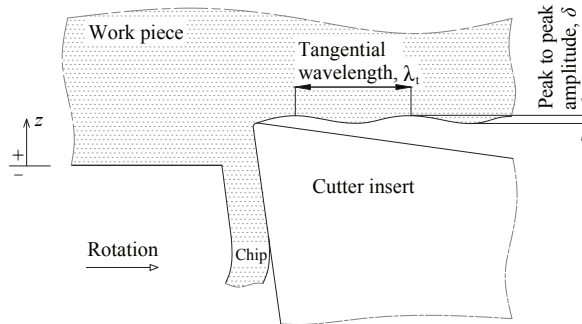


Figure 13: Schematic of generated surface features with a vibration assisted machining.

After the machining tests, surface measurements were conducted at a diametrical location of 110 mm. Surface profile (length of 4 mm in $x$ and $y$ direction with tilt compensation) and surface roughness, $R_a$, (evaluation length of 4 mm in the $x$ direction with tilt compensation) were measured using a stylus profilometer (SV-602 Series 178 from Mitutoyo) and 3-D maps (area of 5 mm × 5 mm) were measured using a 3-D optical scanner (Contour GT from Bruker) as summarised in Figure 14.
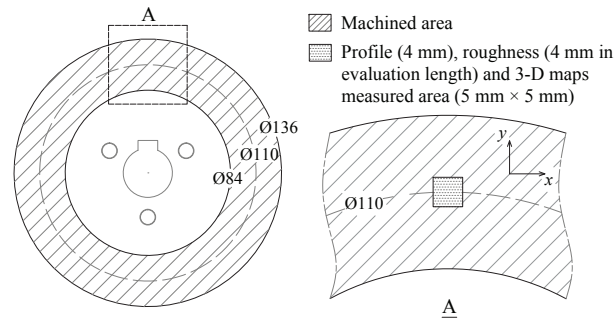
Figure 14: Schematic of the area selected for surface measurement using a stylus profilometer and a 3-D optical scanner.

## 3.2 Results and Discussions

The photographs of the machined surfaces are presented in Figure 15 and Figure 16, 3-D maps in Figure 17, and surface profiles in Figure 18. The tests without vibration, work pieces A1 and S1, demonstrated that smooth surfaces were generated, confirming the stability of the developed device. Overall the vibrations superposed satisfactorily well on the work pieces, and waves of an undulating radial striation pattern were generated on the surfaces of the work pieces A2 to A6 and S2 to S6. The burrs in the diverging area seen on Greco's work[25] were not generated. This was achieved by the continuous engagement of the cutting tool to the work piece surfaces. The sine waves generated through the machining process had peak to peak amplitudes, $\delta$, varying from a few microns to 25 $\mu$m, and the tangential wavelengths, $\lambda_t$, varying from approximately 1 mm to 8 mm.

(a) A1

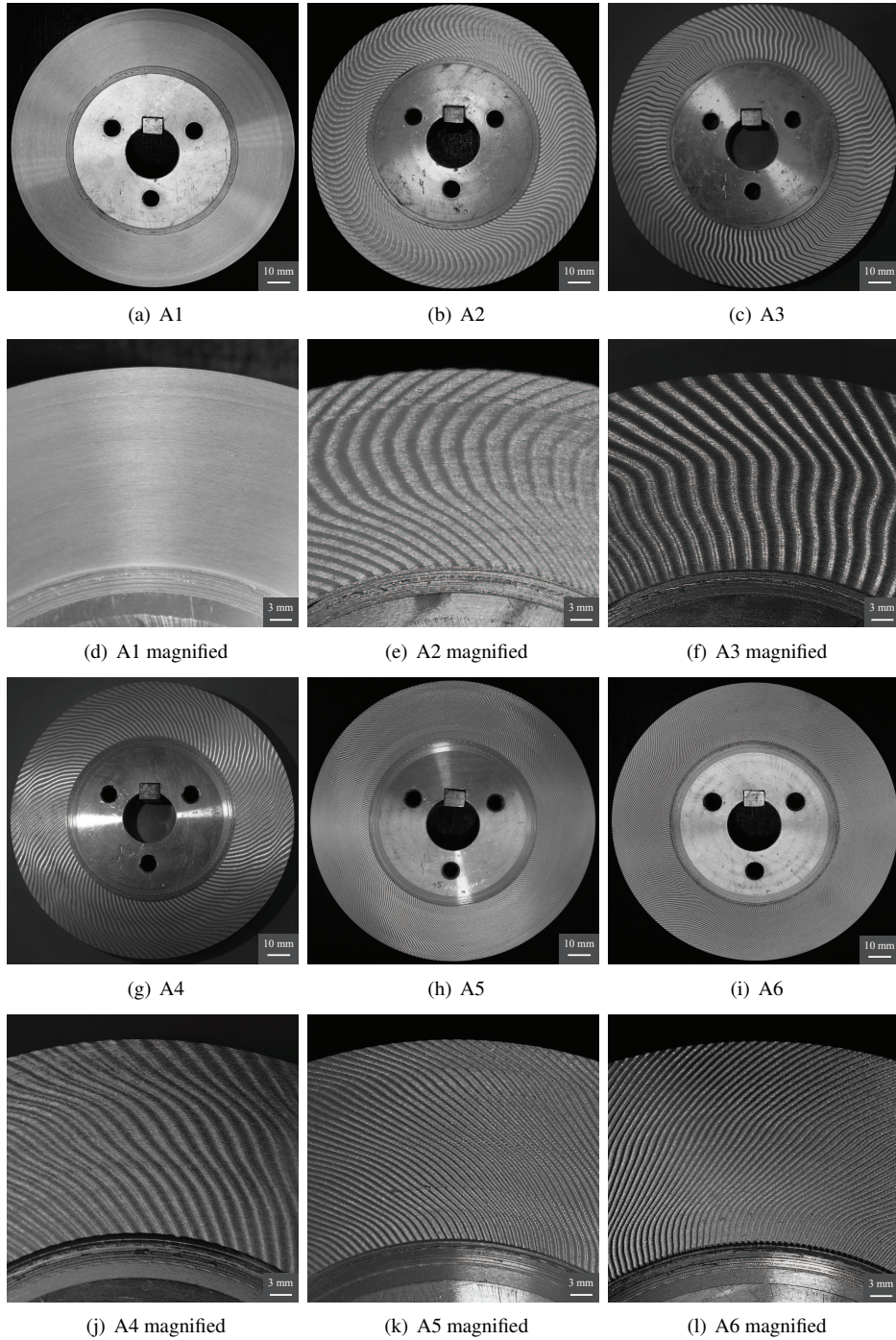(b) A2

(c) A3

(d) A1 magnified

(e) A2 magnified

(f) A3 magnified

(g) A4

(h) A5

(i) A6

(j) A4 magnified

(k) A5 magnified

(l) A6 magnified

Figure 15: Generated textures in work pieces of A1 to A6.

18

(a) S1

(b) S2

(c) S3

(d) S1 magnified

(e) S2 magnified

(f) S3 magnified

(g) S4

(h) S5

(i) S6

(j) S4 magnified

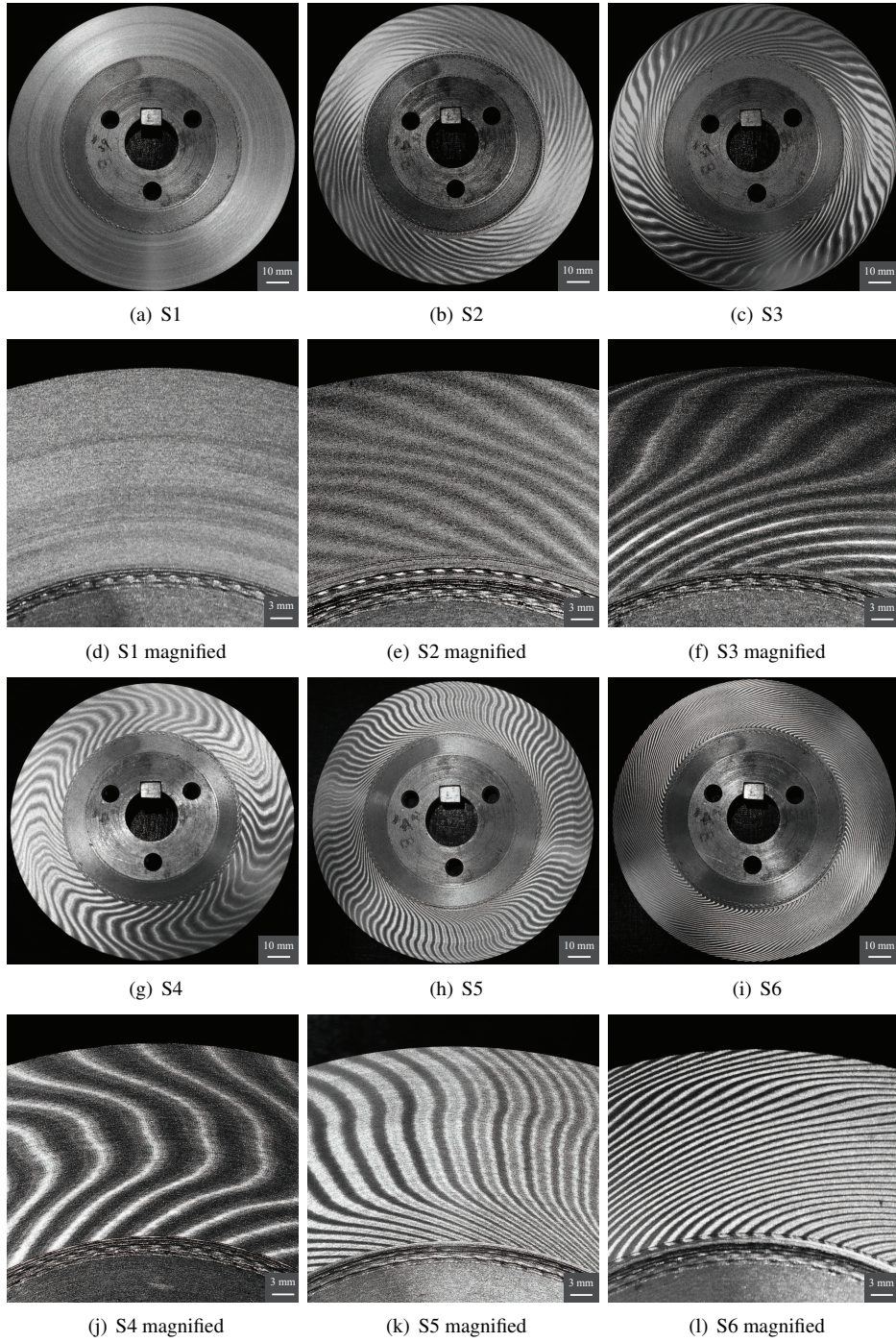(k) S5 magnified

(l) S6 magnified

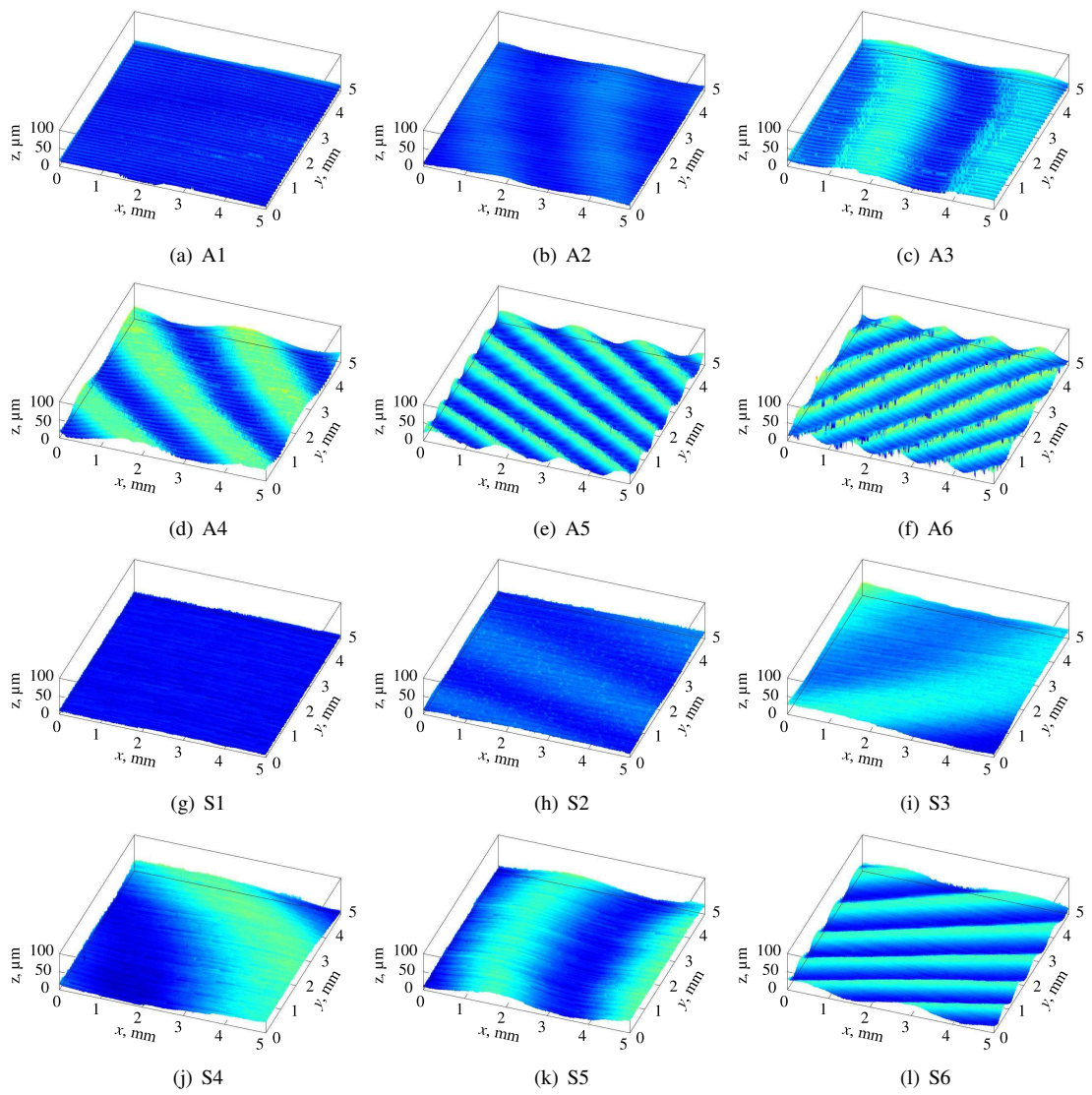Figure 16: Generated textures in work pieces of S1 to S6.

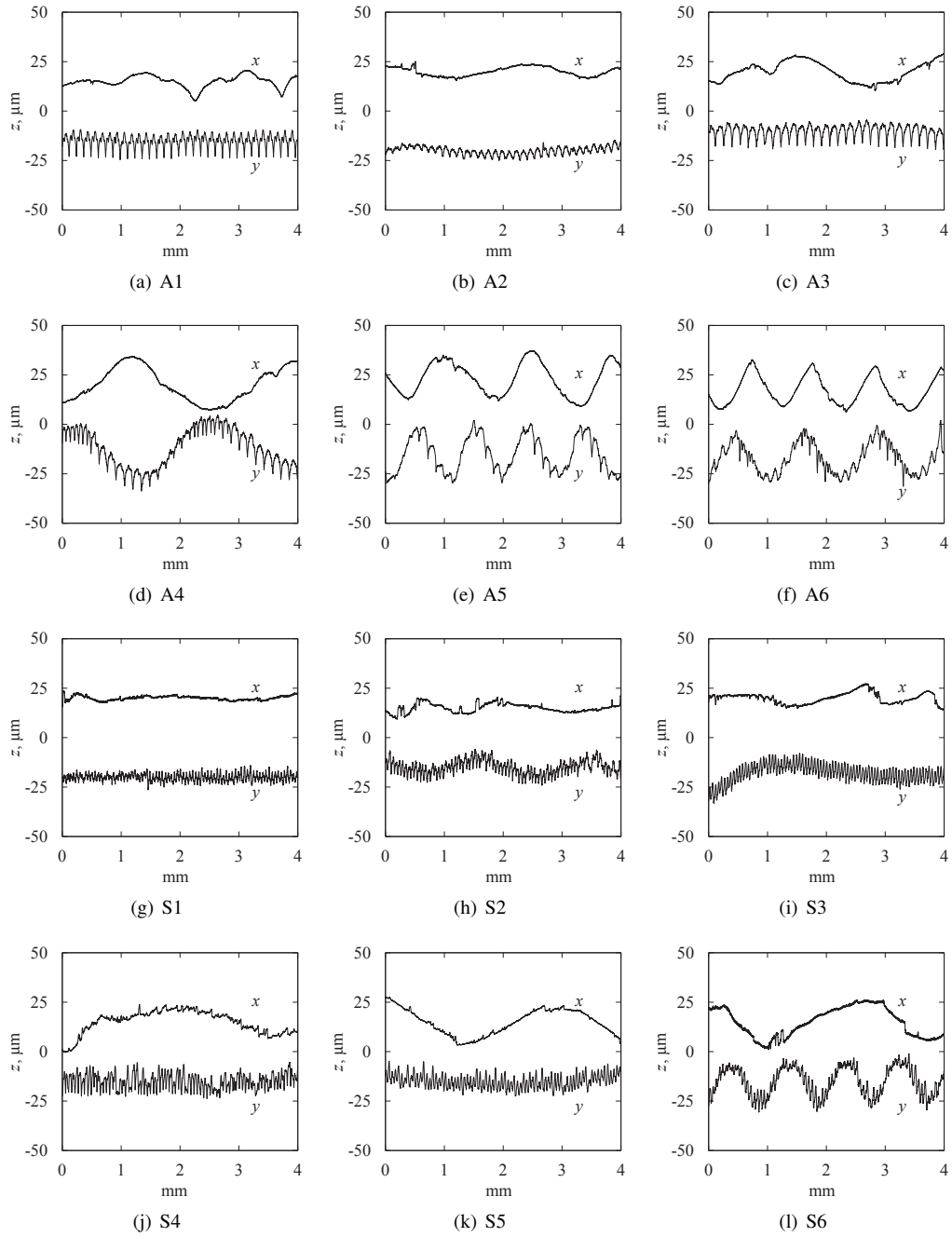Figure 17: 3-D maps measured by 3-D optical scanner in work pieces of A1 to A6 and S1 to S6.

Figure 18: Surface profiles measured by stylus profilometer in work pieces of A1 to A6 and S1 to S6.

### 3.2.1 Generated peak to peak amplitude on surface

Figure 19 presents the generated peak to peak amplitude of surface texture over the displacement of the piezoelectric element measured by the strain gauge in the machined surfaces with vibration. The values of $\delta$ plotted in the graph were read from the obtained 3-D maps.
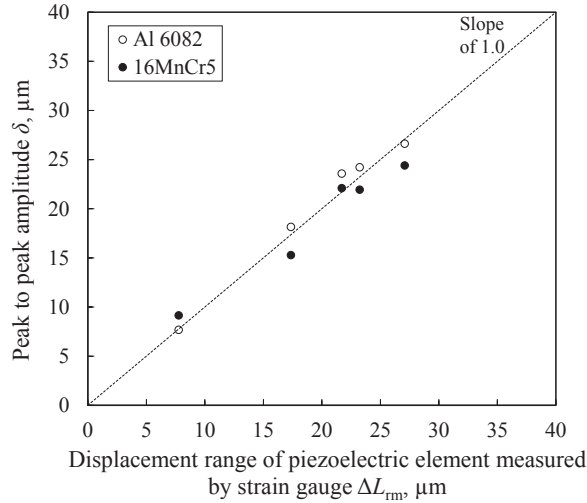


Figure 19: Summary of $\Delta L_{rm}$ and $\delta$ in work piece of A2 to A6 and S2 to S6.

Approximately 8 $\mu$m (A2 and S2) to 25 $\mu$m (A4 and S4) of the peak to peak amplitude were generated on the surfaces. The generated peak to peak amplitude of surface texture showed good agreement with the superposed displacement overall. It is assumed that the amplitudes of the surface textures were accurately generated due to the high axial stiffness of the mechanical components (i.e. cutter insert, cutter shank, and flexible tip) between the work piece and piezoelectric element, so that little deflection occurred. The coefficient of determination, $R^2$, yielded 0.948 with the samples of $\delta$ and the predicted line with slope of 1.0.
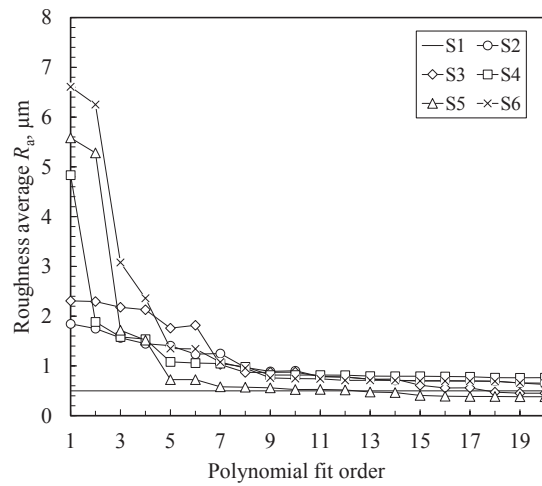
### 3.2.2 Surface roughness

The roughness average, $R_a$, was measured after machining using a stylus profilometer in the tangential direction. For the work pieces without vibration, A1 and S1, an evaluation length of 4 mm with a cut-off length of 0.8 mm was used as $R_a$ was expected less than 2.0 $\mu$m (ISO 4288: 1996). $R_a$ of 1.2 $\mu$m in the Al 6082 and 0.5 $\mu$m in the 16MnCr5 were obtained, which confirmed the stability of the constructed assembly. For the other work pieces, where waviness was intentionally created (A2 to A6 and S2 to S6), the waviness was removed for the roughness assessment. $1^{st}$ to $20^{th}$ order polynomial lines were fitted to the surface profiles, and the deviation of the measured profiles from the fitted lines integrated across the evaluation length (4 mm). As shown in Figure 20, the obtained $R_a$ values were summarised and compared with the

work pieces without vibration (A1 and S1) for each material investigated. As shown, as the order of the fitted polynomial was increased for a given roughness profile (e.g. for A6), the calculated average surface roughness values converged. In all cases, it was found that the value after convergence was less than 1.0 $\mu$m, indicating a similar level of performance in all of the machining operations once the surface waviness had been removed.
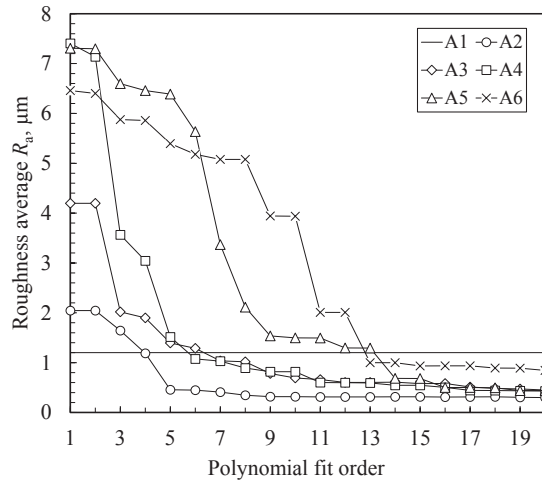


(a) Al 6082



(b) 16MnCr5

Figure 20: Summary of roughness average in $1^{st}$ to $20^{th}$ polynomial fit order.

The data showed that $R_a$ of the underlying surface, once the intentional surface waviness has been removed, is little changed by the use of vibration assisted cutting over the settled order, although it was expected that the roughnesses could be improved by the vibration superposition as seen in a resonant tech-

23

nique by Moriwaki et al[18]. This could be because of the superposed vibration direction and the way of cutting tool engagement. In the study by Moriwaki el al[18], the linear vibration was superposed on to the cutter in the cutting direction and the cutter engaged with the work piece intermittently in ultrasonic frequency range (40 kHz). While in this study the vibration was superposed normal to the face of the work piece and the cutter engaged with the work piece continuously along the sinusoidal displacement, which could have acted as the conventional cutting engagement.

### 3.2.3  Phase shift

The turned surface on the disc has the form of a helical spiral. In the vibration assisted machining process described in this paper, long range waviness is superimposed on top of this topography. As shown in Figure 21 (left), when the rotational speed of the work piece is in phase with the vibration frequency of the actuator, the developed surface texture will be in phase between coincident cutter paths as the tool moves radially inwards, resulting in visible radial striations on the surface.
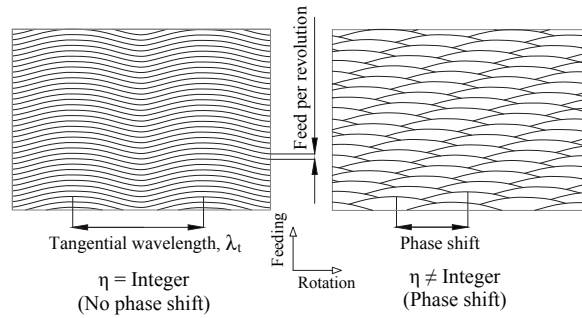


Figure 21: Schematic of textures with a phase shift and with no phase shift.

Conversely if the process is out of phase, an interference pattern occurs (Figure 21 (right)). This is summarised in Equation (13), where $\eta$ represents the phase shift, and $f$ and $\omega$ the vibration frequency and spindle rotation speed respectively. Where $\eta$ is an integer, the system is said to be in phase.

$$\eta = \frac{60f}{\omega}. \tag{13}$$

This effect was further explored in test piece A7 (Figure 22), which was machined with a phase shift deliberately introduced ($f$ = 401 Hz and $\omega$ = 200 rpm as presented in Table 5). As shown in Figure 22(b), the surface profile of this specimen was subsequently measured, and the previously described interference pattern was evident. However, as shown in Figure 15 and 16, undulating radial patterns were also visible on work pieces A2 to A6 and S2 to S6, which were produced with the system nominally in phase. These samples were markedly different in appearance to A7, and the phase appeared subject to low frequency variations. Further investigation of the test set-up indicated that this was due to a varying speed output from

the spindle, as it did not have a feedback controller. This was confirmed in subsequent research work into the application of the technique, where a journal bearing shell was machined on a CNC turning machine with the device (Figure A1 in Appendix). The turning machine used in this case had an accurate speed controller on the spindle, and phase shifts were not evident on the machined specimen (Figure A2).


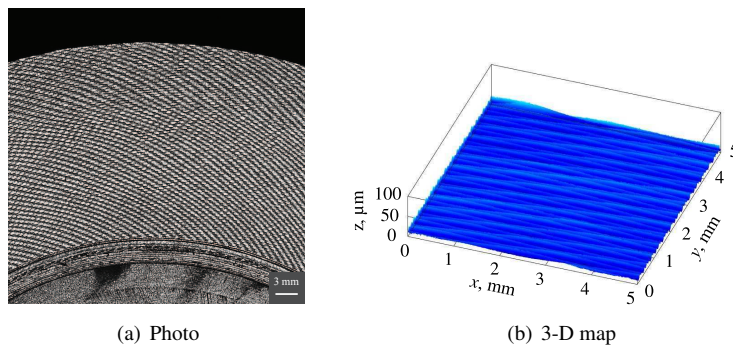
(a) Photo

(b) 3-D map

Figure 22: Generated surface texture with a phase shift in work piece of A7.

## 4    Conclusions

A novel variant of non-resonant vibration assisted machining technique has been investigated to create bespoke surface textures in a conventional milling machine. The following conclusions are drawn from this study:

- A non-resonant vibration assisted machining device has been constructed using an off-the-shelf piezo-electric actuator, its control system, and a conventional cutting tool. The geometry of the constructed mechanical assembly was compact, 199 mm in height and 80 mm in outer diameter. The assembly required a small space to set up in the milling machine and could be easily arranged on other machining platforms, e.g. in a turning machine with a simple adapter.

- The feasible operational range with interaction of the cutting force was discussed with a focus of pull force limitation of the preload spring. In high frequency operation range the dynamic force was predominantly greater than the cutting force which was approximated as a conventional cutting process with a varying depth of cut.

- The vibration commanded on the work pieces corresponded well to the textures generated on the surfaces with regards to frequency and amplitude of the wave forms with no burr generation. This was achieved by the limitation of the elastic deflection effect of the developed mechanical assembly due to the high axial stiffness and the continuous engagement of the cutting tool to the work piece surface. Surface textures consisting of a repeating radial striation pattern of sine waves were reproducibly generated when the frequency of the superposed vibration was in phase with the rotational speed of

the work piece. The generated sine wave were controllable from approximately 1 mm to 8 mm in the wavelength and from a few microns to 25 $\mu$m in the peak to peak amplitudes which would reasonably cover the range of hydrodynamic lubrication film thickness.

- The work pieces were also machined without vibration, and smooth surfaces with a roughness average in tangential direction, $R_a$ of 1.2 $\mu$m in the Al 6082 and 0.5 $\mu$m in the 16MnCr5 were obtained, confirming the stability of the test rig developed. Once the waviness of the surface profile was filtered out, $R_a$ of work pieces generated with vibration were almost as smooth as those without vibration.

- A machining test where a phase shift was deliberately introduced between the vibration frequency and the spindle rotation speed was examined. The result was that the radial striation patterns seen on the work pieces in which the system was nominally in phase were not created, instead an interference pattern occurred.

This machining process which took 52 s for a work piece is a rapid, and relatively inexpensive method for creating bespoke surface textures. Such surfaces may have applications in the field of tribology, as a method for enhancing hydrodynamic lubricant film formation. Further investigation can be directed toward the implementation of the constructed device in machinings with deeper depth of cut on a hardened material where the push force could limit the operation range. The investigation of contributory factors for the minor phase shift could also be an area of the future study.

## Acknowledgement

# References

1. Sy-Wei Lo and Tzu-Chern Horng. Lubricant permeation from micro oil pits under intimate contact condition. *Journal of tribology*, 121(4):633–638, 1999.

2. Ulrika Pettersson and Staffan Jacobson. Influence of surface texture on boundary lubricated sliding contacts. *Tribology International*, 36(11):857–864, 2003.

3. DB Hamilton, JA Walowit, and CM Allen. A theory of lubrication by microirregularities. *Journal of Fluids Engineering*, 88(1):177–185, 1966.

4. Xiaolei Wang, Koji Kato, Koshi Adachi, and Kohj Aizawa. Loads carrying capacity map for the surface texture design of SiC thrust bearing sliding in water. *Tribology International*, 36(3):189–197, 2003.

5. André Schade, Stefan M Rosiwal, and Robert F Singer. Tribological behaviour of 100 and 111 fibre textured CVD diamond films under dry planar sliding contact. *Diamond and related materials*, 15(10): 1682–1688, 2006.

6. E Lugscheider, K Bobzin, and K Lackner. Investigations of mechanical and tribological properties of CrAlN+ C thin coatings deposited on cutting tools. *Surface and Coatings Technology*, 174:681–686, 2003.

7. R Ruprecht, T Benzler, T Hanemann, K Müller, J Konys, V Piotter, G Schanz, L Schmidt, A Thies, H Wöllmer, et al. Various replication techniques for manufacturing three-dimensional metal microstructures. *Microsystem technologies*, 4(1):28–31, 1997.

8. M Lejeune, Thierry Chartier, C Dossou-Yovo, and R Noguera. Ink-jet printing of ceramic micro-pillar arrays. *Journal of the European Ceramic Society*, 29(5):905–911, 2009.

9. Nerea Otero, Pablo Romero, Alejandro Gonzalez, and Alessandra Scano. Surface texturing with laser micro cladding to improve tribological properties. *JOURNAL OF LASER MICRO NANOENGINEERING*, 7(2):152–157, 2012.

10. Mark C Malburg, Jay Raja, and David J Whitehouse. Characterization of surface texture generated by plateau honing process. *CIRP Annals-Manufacturing Technology*, 42(1):637–639, 1993.

11. CM Waits, Brian Morgan, M Kastantin, and R Ghodssi. Microfabrication of 3D silicon MEMS structures using gray-scale lithography and deep reactive ion etching. *Sensors and Actuators A: Physical*, 119(1):245–253, 2005.

12. KH Ho and ST Newman. State of the art electrical discharge machining (EDM). *International Journal of Machine Tools and Manufacture*, 43(13):1287–1300, 2003.

13. NBAUW Sprang, DBAUW Theirich, and JBAUW Engemann. Plasma and ion beam surface treatment of polyethylene. *Surface and Coatings Technology*, 74:689–695, 1995.

14. G Ryk, Y Kligerman, and Izhak Etsion. Experimental investigation of laser surface texturing for reciprocating automotive components. *Tribology Transactions*, 45(4):444–449, 2002.

15. P Zhang and J Lindemann. Influence of shot peening on high cycle fatigue properties of the high-strength wrought magnesium alloy AZ80. *Scripta Materialia*, 52(6):485–490, 2005.

16. Masatoshi Yoshizaki. Improvement in tooth surface strength of carburized transmission gears by fine particle bombarding process. Proc, 2008.

17. DE Brehl and TA Dow. Review of vibration-assisted machining. *Precision engineering*, 32(3):153–172, 2008.

18. Toshimichi Moriwaki and Eiji Shamoto. Ultraprecision diamond turning of stainless steel by applying ultrasonic vibration. *CIRP Annals-Manufacturing Technology*, 40(1):559–562, 1991.

19. Masahiko Jin and Masao Murakawa. Development of a practical ultrasonic vibration cutting tool system. *Journal of materials processing technology*, 113(1):342–347, 2001.

20. Olaf Dambon, Fritz Klocke, Michael Heselhaus, Benjamin Bulla, Andreas Weber, Ralf Schug, and Bernd Bresseler. Vibration-assisted machining research at Fraunhofer IPT–diamond turning and precision grinding. In *Proceedings of the 23rd Annual Meeting of the American Society for Precision Engineering*, 2006.

21. Toshimichi Moriwaki and Eiji Shamoto. Ultrasonic elliptical vibration cutting. *CIRP Annals-Manufacturing Technology*, 44(1):31–34, 1995.

22. Eiji Shamoto and Toshimichi Moriwaki. Ultaprecision diamond cutting of hardened steel by applying elliptical vibration cutting. *CIRP Annals-Manufacturing Technology*, 48(1):441–444, 1999.

23. J Overcash and J Cuttino. Development of a tunable ultrasonic vibration-assisted diamond turning instrument. In *ASPE Proceedings 2003 Annual Meeting*, pages 503–506, 2003.

24. Nobuhiko Negishi. Elliptical vibration assisted machining with single crystal diamond tools. MS thesis, North Carolina State University, 2003.

25. Aaron Greco, Steven Raphaelson, Kornel Ehmann, Q Jane Wang, and Chih Lin. Surface texturing of tribological interfaces using the vibromechanical texturing method. *Journal of manufacturing science and engineering*, 131(6):061005, 2009.

26. Min S Hong and Kornel F Ehmann. Generation of engineered surfaces by the surface-shaping system. *International Journal of Machine Tools and Manufacture*, 35(9):1269–1290, 1995.

27. Physik Instrumente GmbH and Co. User Manual P-212. `http://pi-sales.ws/index.php?id=830`, Accessed on Feb 2015.

28. Physik Instrumente GmbH and Co. User Manual E-481. `http://pi-sales.ws/index.php?id=840`, Accessed on Feb 2015.

29. Sandvik Coromant Ltd. Turning tools - general turning 2012. `http://www.sandvik.coromant.com/sitecollectiondocuments/downloads/global/catalogues/en-gb/turning/turn_a.pdf`, Accessed on Feb 2015.

30. Mikell Groover. *Principles of modern manufacturing*. John Wiley and Sons, INC, Hoboken, USA, 4th edition, 2011.

31. The Japan Society of Mechanical Engineers. *Mechanical Engineer's Concise Handbook :In Japanese*. Maruzen Co, Tokyo, Japan, 7th edition, 2012.

32. Physik Instrumente GmbH and Co. Catalog: Piezo Nano Positioning 2009, 2009.

## Appendix

### Vibration assisted machining in a turning machine

The constructed device can be set up in a turning machine (Triumph VS2500 from Colchester Harrison) with a simple adapter as shown in Figure A1. The device body bolted with a tool holder and a supporting plate is positioned vertically along a tool slide of the turning machine. The cutter vibrates normal to the shaft work piece (radial direction) and the device is fed along the axial direction of the shaft work piece.

A machining test superposing a sinusoidal vibration in the turning machine arrangement was examined in a mild steel (EN8) shaft work piece (98 mm in outer diameter and 58 mm in width split into two journals by a groove at the centre) which represents a journal bearing of an automotive transmission. The machining test was conducted at; 400 rpm in rotation speed, 0.4 mm/s in feed speed, 50 $\mu$m in initial depth of cut, 600 Hz in vibration frequency, and 4 V in voltage range commanded to voltage source. The $x$ coordinate is the tangential direction of the shaft work piece, the $y$ coordinate is the axial direction of the shaft work piece, and the $z$ coordinate is the vibration direction, i.e. the radial direction of the shaft work piece, respectively.
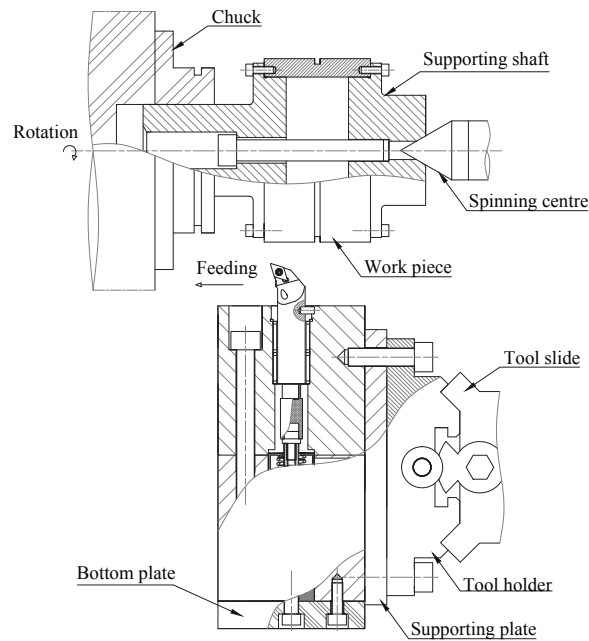


Figure A1: Mechanical arrangement in turning machine.

Photograph of the machined surfaces and 3-D map are presented in Figure A2. The vibration superposed satisfactorily well on the surface and a repeating sinusoidal waves was generated as seen in the disc work pieces. The created pattern was consistent throughout the machined surface without the minor phase shift which was seen in the disc work pieces. This could be achieved by the stable rotation speed of spindle and the less mechanical clearance of the work piece arrangement.
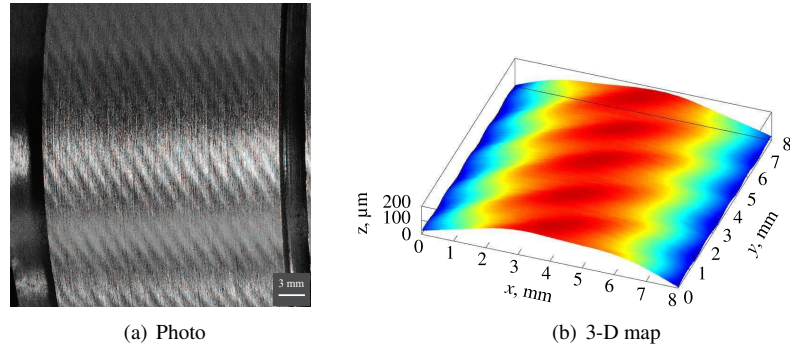
(a) Photo
(b) 3-D map

Figure A2: Generated surface texture of the shaft work piece in the turning machine arrangement.

## Nomenclature

| | |
|---|---|
| $A$ | Area of chip |
| $f$ | Vibration frequency |
| $f_{res}$ | First resonant frequency |
| $F_t$ | Tangential force of cutting |
| $F_f$ | Feed force of cutting |
| $F_n$ | Normal force of cutting |
| $F_{push}$ | Push force of piezoelectric actuator |
| $F_{pull}$ | Pull force of piezoelectric actuator |
| $F'_{push}$ | Push force capacity of piezoelectric actuator |
| $F'_{pull}$ | Pull force capacity of piezoelectric actuator |
| $K_s$ | Specific cutting force |
| $m$ | Mass of piezoelectric element |
| $m_{eff}$ | Effective mass |
| $M$ | Mass driven by piezoelectric actuator |
| $R^2$ | Coefficient of determination |
| $R_a$ | Roughness average |

| $t$ | Time |
|---|---|
| $t_0$ | Initial depth of cut |
| $t_d$ | Depth of cut |
| $u_f$ | Feed speed |
| $u_{fpr}$ | Feed per revolution |
| $V_e$ | Operating voltage of piezoelectric element |
| $V_m$ | Mean voltage commanded to voltage source |
| $x$ | Coordinate in tangential direction of disc work piece |
| $y$ | Coordinate in radial direction of disc work piece |
| $z$ | Coordinate in vibration direction |
| $z_0$ | Initial position of cutter tip in z coordinate |
| $z_c$ | Dynamic position of cutter tip in z coordinate |
| $\delta$ | Peak to peak amplitude of surface texture |
| $\Delta L$ | Displacement of piezoelectric element |
| $\Delta L'$ | Displacement capacity of piezoelectric actuator |
| $\Delta L_r$ | Displacement range of piezoelectric element |
| $\Delta L_{rm}$ | Displacement range of piezoelectric element measured by the strain gauge |
| $\Delta L_{rt}$ | Displacement range of cutter tip |
| $\Delta V$ | Voltage range commanded to voltage source |
| $\eta$ | Ratio of vibration frequency and rotation speed of spindle |
| $\kappa_a$ | Stiffness of piezoelectric actuator |
| $\kappa_e$ | Stiffness of piezoelectric element |
| $\kappa_{sp}$ | Stiffness of preload spring |
| $\lambda_t$ | Tangential wavelength of texture |
| $\omega$ | Rotation speed of spindle |